# The influence of peak-locking errors on turbulence statistics computed from PIV ensembles

**K. T. Christensen**

**Abstract** The influence of peak-locking errors on turbulence statistics computed from ensembles of PIV data is considered. PIV measurements are made in the streamwise–wall-normal plane of turbulent channel flow. The PIV images are interrogated in three distinct ways, generating ensembles of velocity fields with absolute, moderate, and minimal peak locking. Turbulence statistics computed for all three ensembles of data indicate a general sensitivity to peak locking in the single-point statistics, except for the mean velocity profile. Peak-locking errors propagate into the fluctuations of velocity, rendering single-point statistics inaccurate when severe peak locking is present. Multi-point correlations of both streamwise and wall-normal velocity are also found to be influenced by severe levels of peak locking. The displacement range of the measurement, defined by the PIV time delay, appears to affect the influence of peak-locking errors on turbulence statistics. Smaller displacement ranges, particularly those that produce displacement fluctuations that are less than one pixel in magnitude, yield inaccurate turbulence statistics in the presence of peak locking.

# 1
# Introduction

Over the past few years, particle-image velocimetry (PIV) has become the experimental tool of choice for the measurement of velocity in both industry and academia. Hence, PIV is increasingly used to study very complex flow phenomena, including turbulent flows. One of the main advantages of PIV compared to other velocimetry tech-

K. T. Christensen (✉)
Department of Mechanical Engineering,
The University of New Mexico, Albuquerque,
NM 87131-0001, USA
E-mail: ktc@uiuc.edu

*Present address*: K. T. Christensen
Department of Theoretical and Applied Mechanics,
University of Illinois at Urbana-Champaign,
Urbana, IL 61801, USA

niques is that it allows the direct measurement of either two- or three-dimensional instantaneous velocity vectors over a planar domain. Therefore, PIV velocity ensembles are ideal for computing multi-point spatial statistics, quantities particularly crucial for understanding the kinematics and dynamics of turbulent flows.

As with all measurement techniques, there are several uncertainties that can, if not mitigated, degrade the quality of a PIV experiment. Such uncertainties can generally be classified as either random errors or bias errors (Christensen and Adrian 2002). Random errors in PIV are most often associated with electronic noise in the cameras, shot noise (which is independent from pixel to pixel and in time), and random errors associated with properly identifying the sub-pixel displacement. Certainly these errors can play a crucial role in the accuracy of *instantaneous* PIV results. However, due to the random nature of these uncertainties, they can be rendered negligible when the PIV fields are averaged in either space or time over a suitably large ensemble. Therefore, random errors do not degrade the accuracy of statistics derived from larger PIV velocity ensembles and are not considered in the present analysis. [A detailed discussion of PIV measurement errors can be found in Westerweel (1997), Huang et al. (1997), and Christensen and Adrian (2002)].

Bias errors, on the other hand, are certainly not random in space and time and can therefore degrade not only the accuracy of instantaneous PIV results but also any statistic computed from biased PIV ensembles. Several bias errors can exist in a PIV measurement, including uncertainties associated with the fill ratio of the CCD camera and the algorithm used to interrogate the images. However, one of the most significant bias errors associated with a PIV measurement is peak locking (also referred to as "pixel locking" in the literature) –the biasing of particle displacements toward integer pixel values. Peak locking is attributable to both the choice of sub-pixel estimator and under-resolved optical sampling of the particle images. Westerweel (1997) showed that a Gaussian sub-pixel estimator is superior to both centroid and quadratic fits in terms of mitigating peak-locking effects. More recently, Roesgen (2003) presented evidence that a "sinc" interpolation kernel completely suppresses spurious spectral sidelobes in the correlation, yielding minimal peak-locking influences for adequately resolved particle images.

However, when the particle images are under-resolved ($d_\tau/d_{\text{pix}}<2$), peak locking can be a significant bias error that is independent of the choice of sub-pixel estimator. In such cases, the resulting correlation peak is not adequately

**Fig. 1.** Ensemble-averaged probability density function of particle-image displacement illustrating pixel-locking effects

resolved and the sub-pixel estimator cannot faithfully determine the sub-pixel displacement of the particles. Instead, the estimated displacements are "locked" toward integer pixel values. For example, for a true mean particle displacement of 14.35 pixels, the sub-pixel estimator will "lock" the estimated displacement closer to 14 pixels. On the other hand, a true mean particle displacement of 14.65 pixels would be estimated closer to 15 pixels. Therefore, true displacements that exist between integer pixel values are inevitably pushed toward the nearest integer pixel displacement, severely degrading the accuracy of the sub-pixel estimate. This effect can be seen clearly in the ensemble-averaged probability density function (pdf) of the displacement – peaks occur at integer pixel displacements and troughs exist in between. Figure 1 illustrates such behavior.

In a PIV measurement of turbulence, the velocity fluctuations imposed by the turbulence can be small. In turbulent channel flow, the focus of the present effort, the streamwise fluctuations are nearly 10% of the streamwise mean flow, while the wall-normal fluctuations are roughly 5% of the mean flow. Hence, the displacement range associated with the mean flow effectively defines the displacement range of both the streamwise and wall-normal fluctuations. For example, given a mean flow with an average displacement of 10 pixels, the streamwise displacement fluctuations would be nearly 1 pixel, while the wall-normal fluctuations would be associated with displacements approaching 0.5 pixels. Therefore, accurate determination of these fluctuations hinges solely upon the ability of the sub-pixel estimator to faithfully estimate the sub-pixel displacement of the particle images. Since most turbulence statistics of interest are formed from the fluctuations of velocity, peak-locking bias errors may contribute to inaccuracies in statistics computed from PIV ensembles. This paper addresses such issues.

## 2
## Experiment
The PIV experiments central to this study are performed in nominally two-dimensional turbulent channel flow at a bulk Reynolds number of $Re_h=U_bh/v=24{,}000$, equivalently a friction Reynolds number of $Re_\tau=u_*h/v=1{,}184$. Two separate experiments are performed, with the first having a time delay half as large as the second. Two-thousand realizations are acquired per experiment, facilitating

calculation of turbulence statistics with minimal influence of statistical sampling errors. The channel-flow facility is run continuously and the two experiments are performed consecutively in order to minimize differences between the two ensembles due to slightly different flow conditions (specifically Reynolds number and atmospheric conditions). A detailed discussion of the experimental methodology is presented in this section.

## 2.1
## Channel-flow facility
The channel-flow facility is a closed-circuit system, the working fluid is air, and it is driven by a five-horsepower cent-axial blower. Air passes through a flow-conditioning section which includes honeycomb, a series of screens, and a smooth contraction that guides the flow into the 50 mm×600 mm (2h×width, where $h$ is the half-height of the channel) channel cross-section. The flow is tripped upon entrance into the channel with 36-grit sandpaper to ensure fully developed turbulence at the test section. The channel development length is 6.3 m (252 h), including a 1.3-m test section. The flow then returns to the blower through a return section. The test section includes optical access from all directions and static pressure taps are mounted along the length of the channel allowing documentation of the streamwise pressure distribution.

## 2.2
## Flow conditions
In wall-bounded turbulence, the primary velocity scale is the friction velocity, $u_*=(\tau_w/\rho)^{1/2}$. Therefore, determination of $u_*$ requires knowledge of the wall shear stress, $\tau_w$. The wall shear stress can be related to the streamwise pressure gradient through the mean streamwise momentum equation, yielding

$$\tau_w = -\frac{\mathrm{d}P}{\mathrm{d}x}h \qquad (1)$$

for two-dimensional fully-developed channel flow.

Profiles of the streamwise pressure distribution are measured via static pressure taps mounted along the length of the channel development with an inclined manometer having 0.01″ H$_2$0 resolution. The streamwise pressure distribution is linear for the Reynolds number presented here, confirming fully developed two-dimensional flow in the channel and facilitating an accurate estimate of the

streamwise pressure gradient. From this estimate, the wall shear stress is determined using Eq. 1.

The fluid density and viscosity are determined from measurements of the fluid temperature, $T$, and the atmospheric pressure, $P_{atm}$. An ideal gas relation of the form

$$\rho = \frac{P_{atm} + P_{st}}{RT} \tag{2}$$

yields density, where $P_{st}$ is the static pressure at the test location and $R = 279.1$ J/kg K. Sutherland's correlation is used to estimate the kinematic viscosity as

$$v = 1.458 \times 10^{-6} \frac{T^{3/2}}{\rho(T + 110.4)}. \tag{3}$$

Knowledge of the wall shear stress, in concert with the fluid properties, allows estimation of the friction velocity, $u_*$, and the viscous length scale, $y_* = v/u_*$. All flow parameters are summarized in Table 1.

## 2.3
## PIV details

Particle-image velocimetry (PIV) is used to measure instantaneous two-dimensional velocity ($u,v$) fields in the streamwise–wall-normal ($x$–$y$) plane along the channel's spanwise centerline. The air flow is seeded with nominally 1-μm olive oil droplets created by a Laskin nozzle. The 1.28$h$×0.93$h$ (29.8 mm×23.3 mm; width by height) field of view is illuminated with lightsheets formed from a pair of New Wave Research Gemini Nd:Yag lasers. Each laser pulse has a temporal width of 5 ns and 80 mJ of energy. The nominal thickness of the lightsheets in the test section is approximately 200 μm.

The scattered light from the seed particles is imaged onto a 1280×1024 pixel (width by height) TSI PIVCAM 13-8 12-bit CCD camera with frame-straddle capabilities. A 105-mm focal length lens is used to image the particles with an $f$-number of 8. The field of view is minimized to 29.8 mm×23.3 mm in order to maximize the particle-image diameter, $d_\tau$, relative to the pixel size, $d_{pix}$, yielding $d_\tau/d_{pix} \simeq 2$ in both experiments. Further minimization of the field of view is not possible because the width of the channel (600 mm) does not allow camera placement any closer than 300 mm from the lightsheet.

Two distinct images are acquired per vector field with a fixed time delay, facilitating two-frame cross-correlation analysis of the images. As noted earlier, two distinct experiments are performed. The first experiment is performed with a time delay of 10 μs. (This experiment is hereafter referred to as "experiment A".) The second experiment is performed with a time delay of 20 μs. (The second experiment is hereafter referred to as "experiment B".) The second experiment is performed specifically to study the influence of a larger displacement range on

peak-locked data and on the turbulence statistics computed from such data.

The pairs of PIV images are interrogated using the *PIV Sleuth* software (Christensen et al. 2000). The images are subdivided into rectangular interrogation windows of size 26×20 pixels (width×height) in the first image and 32×24 in the second image. The interrogation windows are zero-padded in 32×32 pixel buffers and the correlations are calculated using FFT methods. A larger second window is chosen to minimize the bias error associated with loss of appropriate image pairs for the particle images defined by the first interrogation window. The images are analyzed with 50% overlap to satisfy Nyquist's criterion and the second window is offset in the mean flow direction by the bulk displacement of the flow (7 pixels for experiment A and 14 pixels for experiment B). These interrogation parameters yield 9,408 vectors per velocity realization over the 29.8 mm×23.3 mm field of view.

The instantaneous vector fields in each ensemble are then validated using objective statistical methods (standard deviation and local magnitude difference comparisons) to remove any erroneous velocity vectors. Holes are filled either with alternative velocity choices determined a priori during interrogation or interpolated in regions where at least 50% of neighbors are present. On average, over 99% of the velocity vectors in a given field are found to be valid *prior* to replacement and interpolation. Therefore, the need for interpolation is minimal. Finally, each vector field is low-pass filtered with a narrow Gaussian filter to remove any noise associated with frequencies larger than the sampling frequency of the interrogation. Table 2 summarizes the resolution of the PIV experiment.

## 3
## Image ensembles

As noted in the introduction, two different effects can contribute to the degree of peak locking present in a PIV ensemble. The first influence is associated with under-resolved optical sampling of the particle images. As noted by Westerweel (1997), particle-image diameters less than 1.5 pixels yield a certain level of peak locking, owing to the inability of the sub-pixel estimator to accurately estimate the sub-pixel displacement of the particles. This effect can be exacerbated by the choice of sub-pixel estimator, with quadratic estimators yielding significantly more peak locking than Gaussian estimators (Westerweel 1997). The net effect of both inadequate resolution of the particle images and the choice of sub-pixel estimator is a biasing of the particle displacements toward integer pixel displacements. The field of view in the present experiment is chosen to minimize the influence of under-resolved optical sampling of the particle images. The mean particle-image diameter of the

**Table 1.** Summary of flow parameters

| $Re_\tau$ | $\rho$ (kg/m$^3$) | $v$ (m$^2$/s) | d $P$/d $x$ (Pa/m) | $\tau_w$ (Pa) | $u_*$ (m/s) | $y_*$ (μm) |
|---|---|---|---|---|---|---|
| 1,184 | 1.016 | 1.800×10$^{-5}$ | −29.6 | 0.734 | 0.853 | 21.1 |

**Table 2.** Resolution of the PIV experiment

| $\Delta x$(μm) | $\Delta x$(μm) | $\Delta z$ (μm) | $y_{min}$ (μm) |
|---|---|---|---|
| 304 (14.4$y_*$) | 234 (11.1$y_*$) | 200 (9.5$y_*$) | 398 (19.9$y_*$) |

experiments discussed herein is $d_\tau/d_{\mathrm{pix}}=2$, meaning any peak locking evident in the velocity data can be attributed to the choice of sub-pixel estimator.

The image data in each experiment is interrogated in two ways, once with a quadratic sub-pixel estimator and again with a Gaussian sub-pixel estimator. The former (hereafter referred to as "case I") yields moderately peak-locked velocity data, while the latter (hereafter referred to as "case II") yields velocity data minimally influenced by peak locking. A third ensemble of velocity data in each experiment is created by rounding the displacements in each Gaussian-interrogated velocity field to the nearest integer. This case will hereafter be referred to as "case 0" and is equivalent to using no sub-pixel estimator during interrogation. Hence, case 0 simulates the limiting case of absolute peak locking.

## 3.1
### Experiment A

The ensemble- and area-averaged probability density functions (pdf's) of the streamwise displacement for all three cases of experiment A (smaller displacement range) are shown in Fig. 2a. The streamwise displacements in experiment A span a range of 0 to 10 pixels. In case 0A, the absolute peak-locking limit, displacements are completely "locked" onto integer pixel values. The pdf for case IA (quadratic estimator) is certainly not as severe as case 0A; however, it does show significant peak locking associated with the choice in sub-pixel estimator: displacements are consistently "locked" onto integer pixel displacements. Between the integer-displacement peaks there exist troughs, owing to the shifting of particle displacements toward integer pixel values. Finally, case IIA (Gaussian estimator) clearly illustrates the reduction in peak locking associated with using a Gaussian estimator instead of a quadratic estimator. Minimal peak locking is evident in the case IIA pdf of streamwise displacement, validating

that the particle images have been properly resolved in the present experiment.

The ensemble- and area-averaged pdf's of the wall-normal displacement in experiment A are shown in Fig. 2b for all three cases. The dynamic range of the wall-normal displacements for experiment A is 2 pixels, from $-1$ to 1 pixel. Again, in the limit of absolute peak locking (case 0A), all wall-normal displacements are completely locked onto integer values of $-1$, 0, and 1. Additionally, peak-locking effects are also noted in case IA (quadratic estimator) near these same integer values, although they are not as severe as in case 0A. Case IIA (Gaussian) shows no influence from peak locking, just like the streamwise displacement of case IIA. The most notable observation in the pdf's of wall-normal displacement for experiment A is the biasing of displacements toward zero displacement. The zero-displacement value of the case 0A pdf is six times larger than case IIA, while the zero-displacement value of case IA is twice as large as case IIA. This bias toward zero displacement may lead to underestimation of statistics involving the wall-normal velocity.

## 3.2
### Experiment B

Figure 3a illustrates the ensemble- and area-averaged streamwise displacement pdf's computed from the data of experiment B (larger displacement range) for all three cases. The streamwise displacement dynamic range for experiment B is 0 to 20 pixels. Case 0B illustrates the absolute peak-locking limit, with displacements completely locked onto integer values. As with case IA, case IB exhibits moderate peak locking due to the quadratic sub-pixel estimator. Case IIB shows minimal peak-locking influences. These peak-locking trends are consistent with the behavior of the three cases associated with experiment A.

The pdf's of wall-normal displacement for experiment B are presented in Fig. 3b. The range of wall-normal
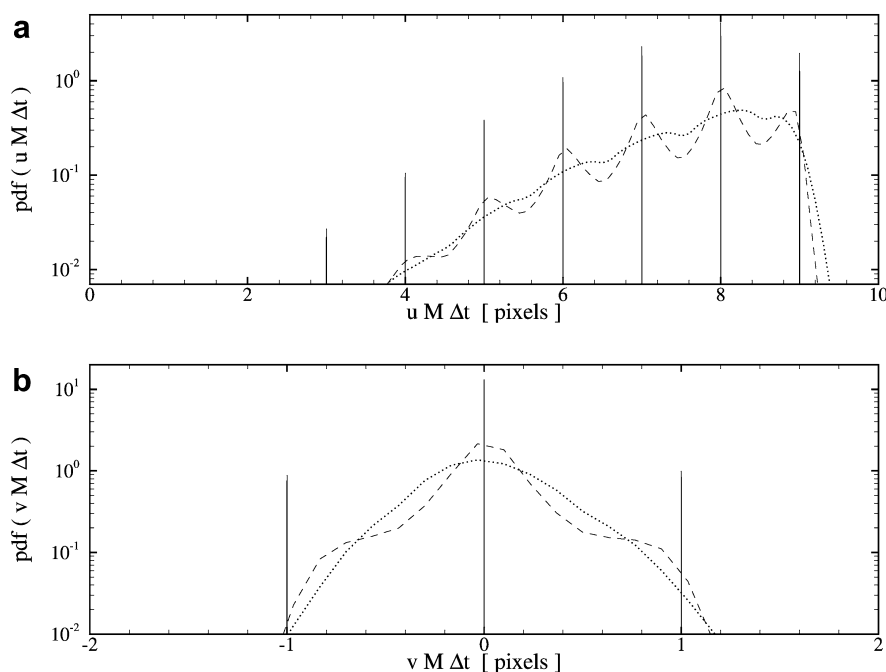
**Fig. 2.** Ensemble- and area-averaged probability density functions of total displacement from experiment A data for **a** streamwise displacement ($uM\Delta t$) and **b** wall-normal displacement ($vM\Delta t$). —: Case 0A (limiting case of absolute pixel locking); – – – : Case IA (quadratic sub-pixel estimator); ⋯: Case IIA (Gaussian sub-pixel estimator)

**a**

pdf ( u M Δt )

u M Δt [ pixels ]

**b**

pdf ( v M Δt )

v M Δt [ pixels ]
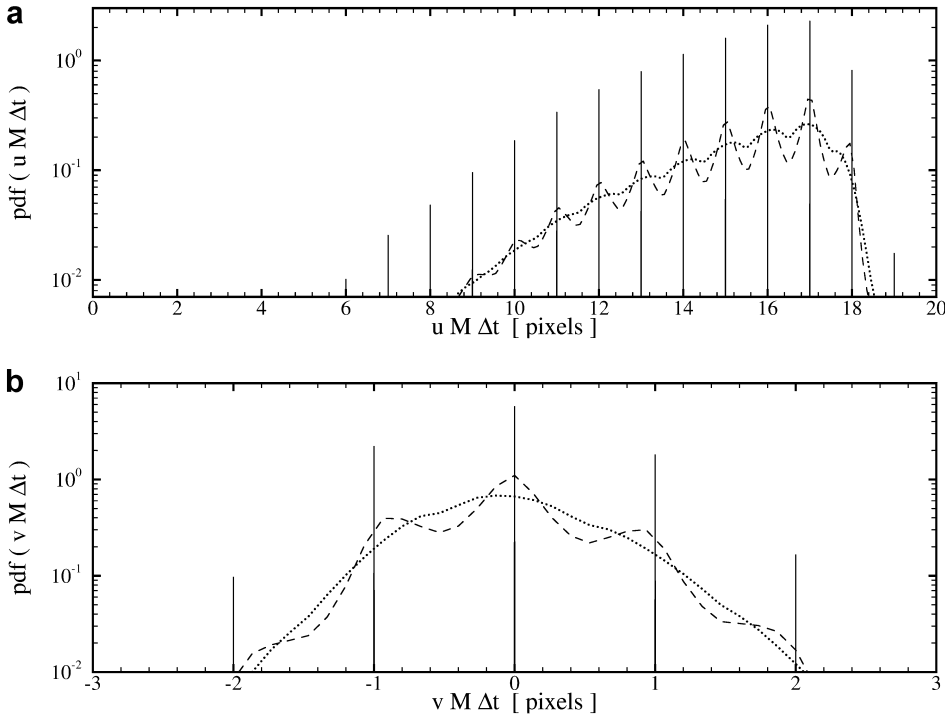
**Fig. 3.** Ensemble- and area-averaged probability density functions of total displacement from experiment B data for **a** streamwise displacement ($uM\Delta t$) and **b** wall-normal displacement ($vM\Delta t$). —: Case 0B; – – – : Case IB; ⋯: Case IIB

displacements for experiment B is 4 pixels, from –2 to 2 pixels. The displacements in case 0B are completely locked onto integer values, while the displacements in case IB are also locked onto these integer displacements, but with far fewer locked toward a magnitude of 2 pixels. Case IIB exhibits no influence of peak locking in the wall-normal displacements. Clearly, however, the wall-normal displacements in experiment B span a broader pixel range than do the wall-normal displacements in experiment A. In particular, there are fewer displacements locked toward zero. Therefore, wall-normal velocity statistics computed from the experiment B data may not be as sensitive to peak locking as statistics computed from the experiment A data.

Two questions still remain: How do peak-locking errors affect turbulence statistics computed from PIV ensembles? Does the dynamic range of the displacements play a role in this effect? The first question is addressed in the next section (Turbulence statistics for experiment A) by considering statistics computed from the velocity ensembles of experiment A. Single- and multi-point statistics computed from the three distinct cases of velocity data are directly compared. The second question is addressed in Sect. 5 (Influence of displacement dynamic range) by comparing the statistics from experiment A to those computed from experiment B.

# 4
# Turbulence statistics for experiment A

## 4.1
## Single-point statistics
We first present single-point statistics computed from the three ensembles of velocity data associated with experiment A: case 0A, case IA, and case IIA. The single-point statistics for each case are computed by ensemble averaging the instantaneous velocity fields followed by line averaging in the streamwise direction since it is homogeneous. This averaging methodology yields profiles that are only a function of wall-normal position ($y$). Since all three ensembles constitute measurements of the same flow events (they are derived from the same image ensemble), any differences in the statistics computed for each case can be interpreted as the influence of varying degrees of peak locking.

### 4.1.1
### Mean velocity
Figure 4 presents the mean velocity, $U^+=U/u_*$, as a function of wall-normal position. All three cases yield identical mean velocity profiles, both close to the wall and in the outer region of the flow. This consistency indicates that the mean velocity is not affected by peak-locking errors, even in the limiting case of absolute peak locking.

### 4.1.2
### RMS velocities
Figure 5a, b illustrates the root-mean-square (RMS) of the streamwise and wall-normal velocities, respectively. The RMS velocities are a measure of the strength of the underlying turbulent fluctuations and the displacements associated with these fluctuations are on the order of 1 to 2 pixels. The RMS streamwise velocity, $\sigma_u$, exhibits some sensitivity to peak-locking errors in cases 0A and IA as compared to case IIA (no peak locking). Case 0A, in particular, deviates significantly from case IIA for all wall-normal locations. This deviation is certainly understandable given that case 0A represents absolute peak locking. In contrast, case IA (quadratic estimator; moderate peak locking) accurately follows case IIA for $y<0.6h$ despite a significant difference in the level of peak locking between the cases. Case IA slightly overestimates $\sigma_u$ for $y>0.6h$.
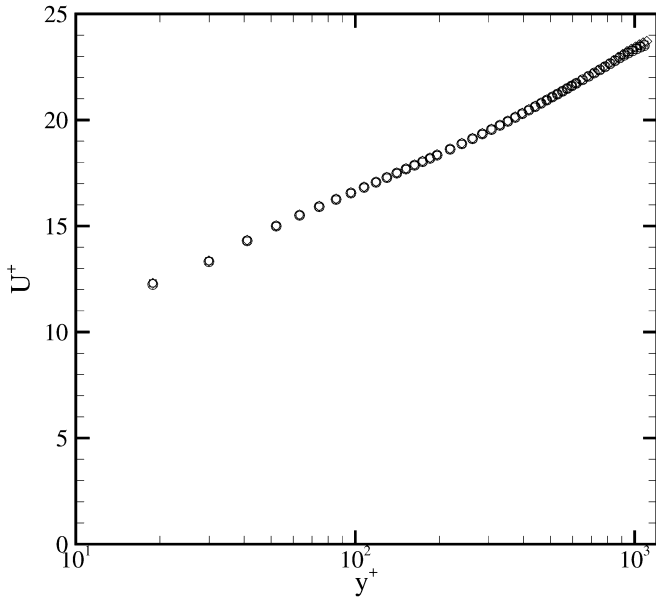
Fig. 4. Inner scaling of mean velocity, $U^+$, versus wall-normal position, $y^+$. ◇: Case 0A; □: Case IA; ○: Case IIA. (Every other data point is removed for clarity.)

The RMS wall-normal velocity, $\sigma_v$, is also sensitive to peak-locking errors. Case 0A overestimates $\sigma_v$ for $y<0.8h$ and underestimates it for $y>0.8h$ as compared to case IIA (no peak locking). In contrast, case IA underestimates $\sigma_v$ at all wall-normal locations, with larger deviations for $y>0.5h$.

Since the mean velocity is unaffected by peak locking, the peak-locking errors present in the total velocity are presumably passed on to the fluctuations of velocity. Therefore, the deviations in $\sigma_u$ and $\sigma_v$ noted in Fig. 5 can be explained by considering the magnitude of the fluctuating displacements. Figure 6a presents ensemble- and line-averaged pdf's of fluctuating streamwise displacements at $y=0.25h$. (These pdf's differ from those shown in Fig. 2 because the latter are ensemble- and area-averaged and represent total, rather than fluctuating, displacements.) The peaks in the pdf's of fluctuating streamwise displacement do not coincide with integer pixel displacements since a non-integer mean has been removed by Reynolds' decomposition. At $y=0.25h$, fluctuating streamwise displacements range from 0 to 2 pixels in magnitude, spanning a displacement range of 4 pixels. Most of the displacements for cases IA and IIA rarely exceed 1.5 pixels in magnitude; however, the streamwise displacements of case 0A are locked toward values as large as 2 pixels in magnitude. Therefore, it should be expected that case 0A would overestimate $\sigma_u$ in this region of the flow, as is noted in the profiles of $\sigma_u$ (Fig. 5a. Figure 6b illustrates pdf's of fluctuating streamwise displacement at $y=0.9h$. In this region of the flow, the fluctuating streamwise displacements have magnitudes between 0.5 and 1 pixel. Therefore, peak-locking influences tend to "lock" these displacements toward 1 pixel, causing overestimation of $\sigma_u$ in cases 0A and IA for $y>0.6h$.

Figure 7a presents ensemble- and line-averaged pdf's of fluctuating wall-normal displacements at $y=0.25h$.

489
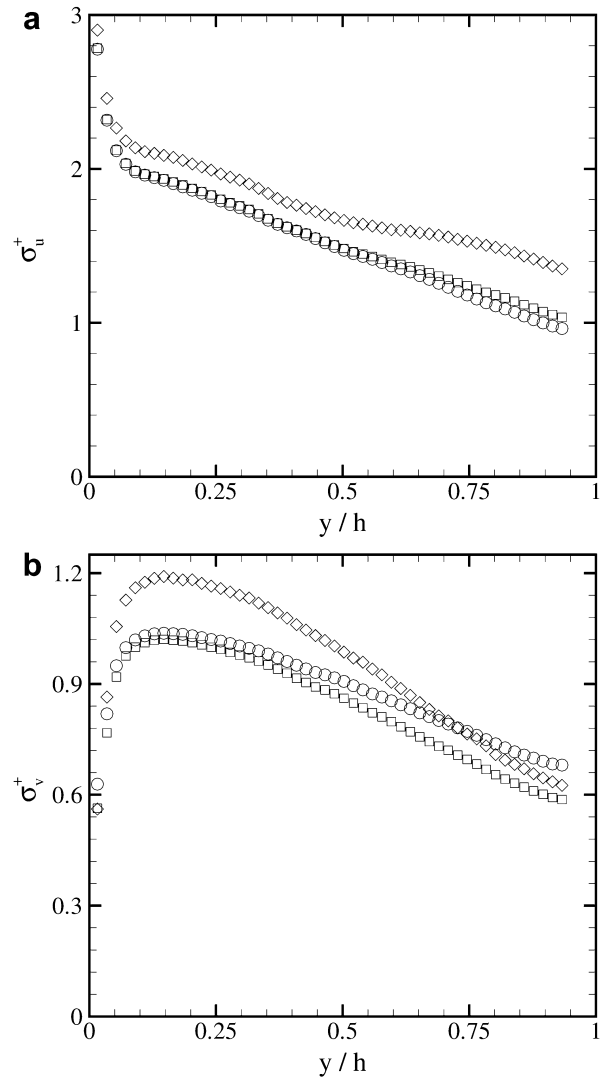




Fig. 5a, b. Profiles of RMS velocity as a function of wall-normal position. a $\sigma_u^+$; b $\sigma_v^+$, ◇: Case 0A; □: Case IA; ○: Case IIA. (Every other data point is removed for clarity.)

Recall that in this region of the flow, case 0A severely overestimates $\sigma_v$. At $y=0.25h$, the fluctuating wall-normal displacements range, in magnitude, from 0 to 1 pixel. In cases IA and IIA, the magnitude rarely exceeds 0.75 pixels, while in case 0A peak-locking influences yield an order of magnitude larger number of displacements locked onto either −1 or 1 pixel. Therefore, these larger fluctuating wall-normal displacements, attributable to peak locking, cause case 0A to overestimate $\sigma_v$ close to the wall. In contrast, near the centerline, it was noted that both cases 0A and IA underestimate $\sigma_v$. Figure 7b illustrates pdf's of fluctuating wall-normal displacement at $y=0.9h$. In this region of the flow, the wall-normal velocity fluctuations are about half as large as they are near the wall, translating into a significant number of fluctuating wall-normal displacements with magnitudes between 0 and 0.5 pixels. In cases 0A and IA, these smaller displacements are "locked" toward zero, yielding an underestimation of $\sigma_v$ as compared to case IIA.

**a**

**b**
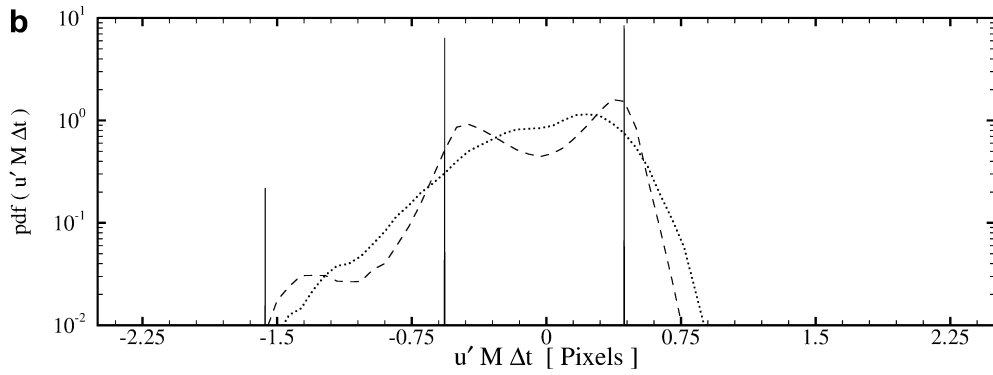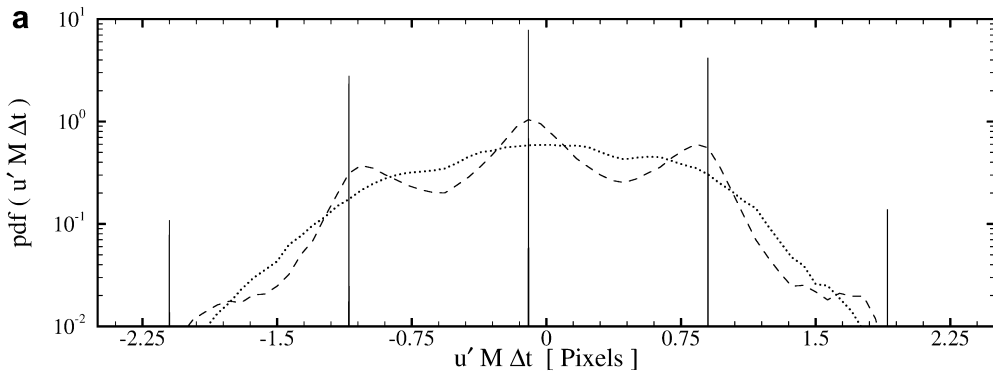
**Fig. 6.** Ensemble-averaged probability density functions of fluctuating streamwise displacement, $u'M\Delta t$, computed from experiment A data at **a** $y=0.25\ h$ and **b** $y=0.9\ h$. —: Case 0A; – – – : Case IA; ⋯: Case IIA



**a**

**b**
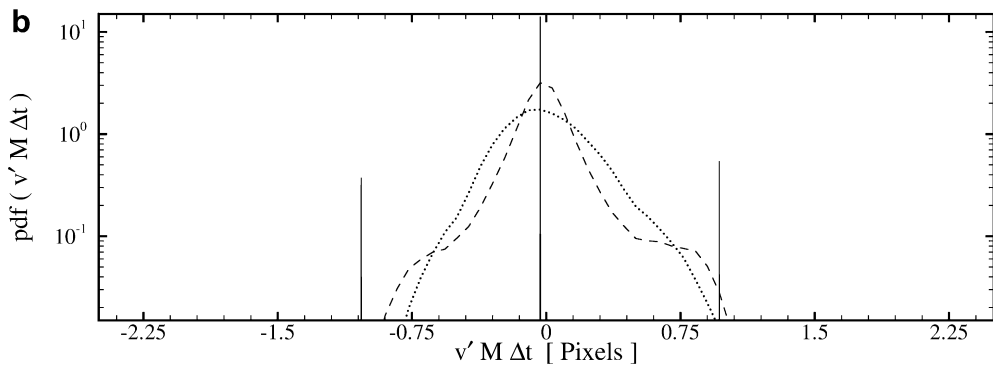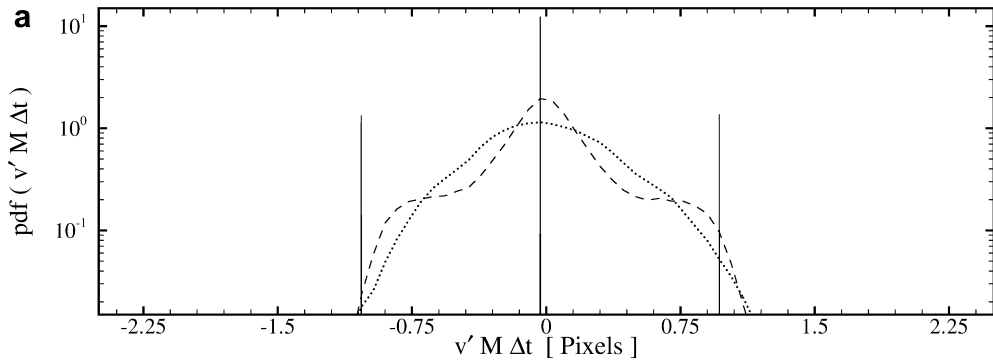
**Fig. 7.** Ensemble-averaged probability density functions of fluctuating wall-normal displacement, $v'M\Delta t$, computed from experiment A data at **a** $y=0.25\ h$ and **b** $y=0.9\ h$. —: Case 0A; – – – : Case IA; ⋯: Case IIA

### 4.1.3
### Reynolds stress

The Reynolds stress, $-\langle u'v'\rangle$, as a function of wall-normal position, is shown in Fig. 8. Case 0A (absolute peak locking) severely underestimates the Reynolds stress compared to cases IA and IIA. This underestimation is attributable to the fact that the peak locking in $u'$ is uncorrelated to the peak locking in $v'$, along with the fact that a majority of the fluctuating wall-normal displacements are locked toward zero in case 0A (see Figs. 6 and 7). The same underestimation is seen in case IA; however, it is not as significant as case 0A since the wall-normal
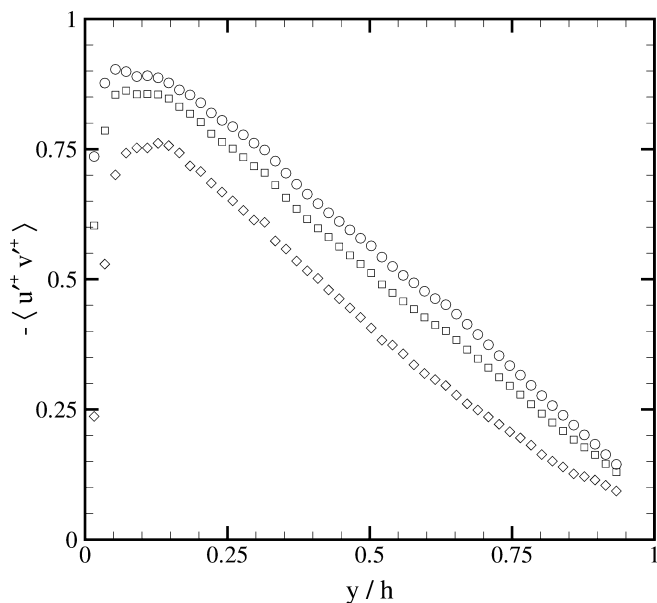
**Fig. 8.** Profiles of Reynolds stress, $-\langle u'^+ v'^+ \rangle$, as a function of wall-normal position. ◇: Case 0A; □: Case IA; ○: Case IIA. (Every other data point is removed for clarity.)
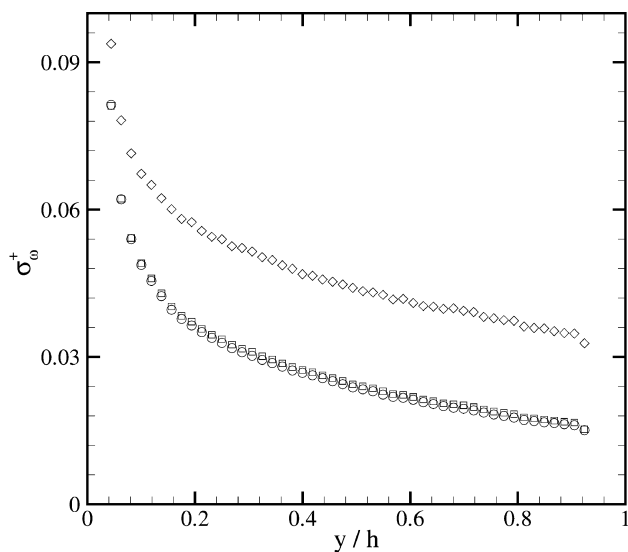


**Fig. 9.** Profiles of RMS spanwise vorticity as a function of wall-normal position. ◇: Case 0A; □: Case IA; ○: Case IIA. (Every other data point is removed for clarity.)

displacement fluctuations are not as severely locked toward zero displacement. Clearly, any "locking" of displacements toward zero severely influences the quality of the Reynolds stress, even more so than the RMS velocities, because $u'$ and $v'$ at a given point must both be locked toward non-zero integer displacements in order to contribute to $-\langle u'v' \rangle$.

### 4.1.4
### Vorticity
Although the comparisons heretofore have been limited to velocity statistics, PIV velocity fields certainly allow the

calculation of other important flow quantities, including vorticity. In-plane vorticity, $\omega_z$, is given by

$$ w_z = \frac{\partial v}{\partial x} - \frac{\partial u}{\partial y}. \tag{4} $$

However, in order to avoid errors associated with differentiating experimental data, in-plane vorticity is calculated for the instantaneous velocity fields in each case using the circulation method (Reuss et al. 1989). The resulting RMS in-plane vorticity profiles as a function of wall-normal position for all three cases are presented in Fig. 9. Clearly, case 0A deviates significantly from the other two cases. This deviation is due to the "locking" of wall-normal displacements toward 0 and 1 pixel (Fig. 15), causing severe discontinuities in $v'$. These discontinuities yield a significant overestimation of $\partial v/\partial x$ and hence $\sigma_\omega$. Case IA actually yields an accurate RMS vorticity profile despite suffering from a moderate level of peak locking. However, the displacements in case IA are relatively smooth compared to case 0A. Therefore, the gradients in velocity in case IA are not tainted by gross overestimation due to discontinuities and are more representative of the actual flow.

### 4.2
### Multi-point statistics
In this section, the influence of peak-locking errors on the accuracy of multi-point statistics is considered. Multi-point statistics play a central role in understanding the kinematics and dynamics of turbulence because they can reflect the influence of coherent vortical structures. For example, the two-point correlation of streamwise velocity in wall turbulence mimics the characteristics of large-scale vortex organization in the outer layer both in terms of inclination angle and streamwise extent (Christensen 2001). In addition, multi-point correlations play a crucial role in development of subgrid-scale models for large-eddy simulation of higher-Reynolds-number turbulence (Langford and Moser 1999).

Two-point velocity correlation coefficients of the form

$$ \rho_{ij}(r_x, y; y_{\text{ref}}) = \frac{\left\langle u_i'(x, y_{\text{ref}}) u_j'(x + r_x, y) \right\rangle}{\sigma_i(y_{\text{ref}}) \sigma_j(y)} \tag{5} $$

are computed from instantaneous fluctuating velocity fields for all three cases. Figure 10a–c presents correlation coefficients ($\rho_{uu}$, $\rho_{vv}$, and $\rho_{uv}$, respectively) as a function of $r_x$ for $y = y_{\text{ref}} = 0.1h$. Cases IA and IIA yield nearly identical results for all three correlations. However, $\rho_{uu}$ and $\rho_{vv}$ computed from case 0A data are underestimated for $r_x \neq 0$. This deviation is attributable to the fact that the correlation coefficients have been normalized by the appropriate RMS velocities as defined in Eq. 5. Since case 0A overestimates both $\sigma_u$ and $\sigma_v$ at $y = 0.1h$, normalization by a larger RMS value yields a smaller correlation coefficient value. As a result, case 0A underestimates both $\rho_{uu}$ and $\rho_{vv}$ for $r_x \neq 0$.

Severe peak locking also underestimates the length scales associated with $\rho_{uu}$ and $\rho_{vv}$. For a fixed correlation coefficient value, the correlations associated with case 0A
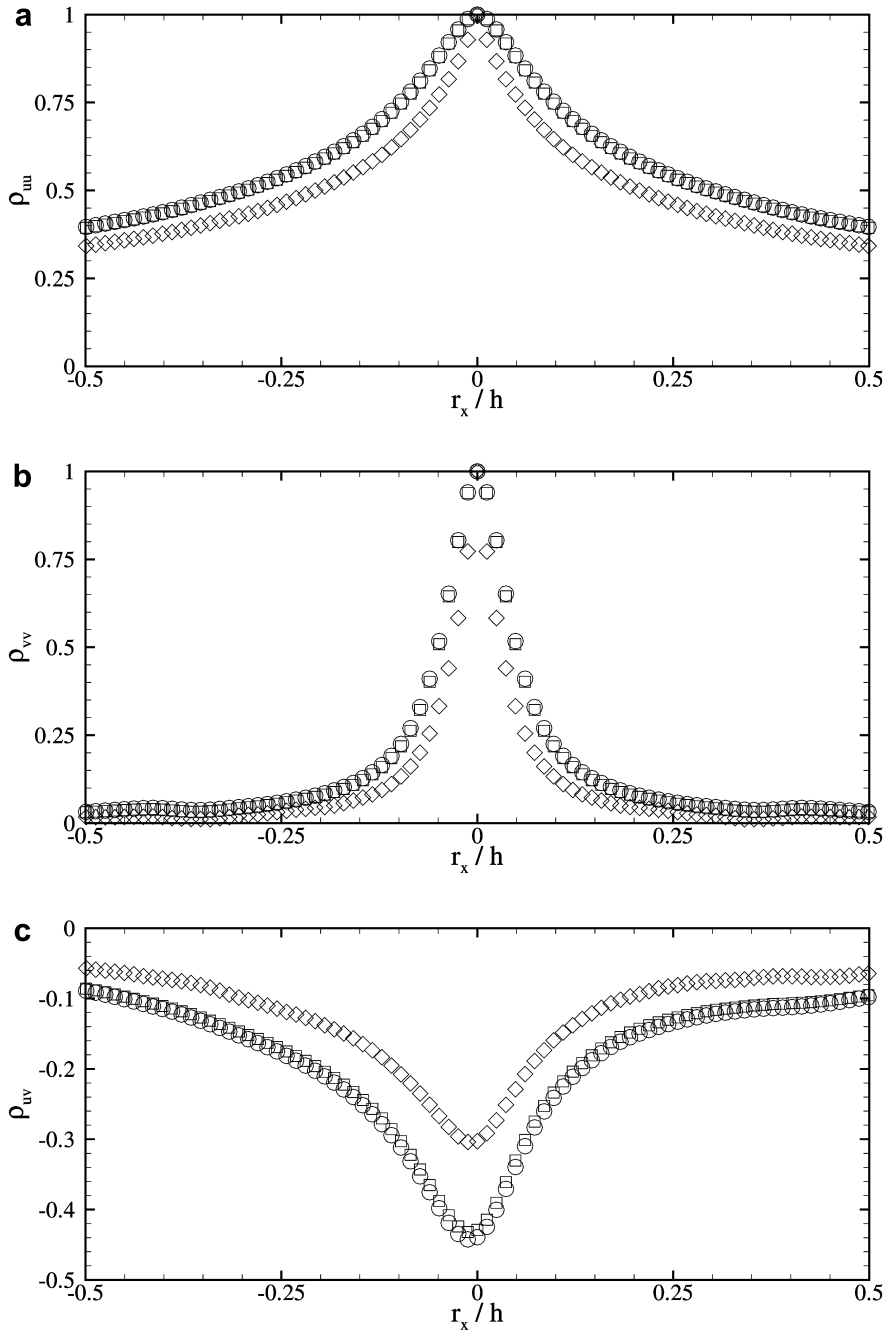
**Fig. 10a–c.** A comparison of two-point velocity correlation coefficients as a function of $r_x$ for $y=y_{\text{ref}}=0.1h$ computed from experiment A data. **a** $\rho_{uu}$; **b** $\rho_{vv}$; **c** $\rho_{uv}$. ◇: Case 0A; □: Case IA; ○: Case IIA

have smaller widths than the correlations computed for cases IA and IIA. In addition, near zero separation, the curvature of $\rho_{uu}$ and $\rho_{vv}$ is consistent between cases IA and IIA, but markedly different for case 0A. Hence, any estimates of the Taylor microscale, defined by this curvature at zero separation, would be inaccurate when computed from severely peak-locked data.

With regard to the cross-correlation, $\rho_{uv}$, case 0A deviates significantly from cases IA and IIA for all values of $r_x$. In particular, the value near zero separation for case 0A is 30% smaller than cases IA and IIA. At zero separation, $\rho_{uv}$ is given by

$$\rho_{uv}(r_x = 0) = \frac{\overline{u'v'}(y)}{\sigma_u(y)\sigma_v(y)}, \tag{6}$$

i.e., the Reynolds stress at $y$ normalized by the RMS velocities of $u$ and $v$ at $y$. Recall that case 0A severely underestimates the Reynolds stress for all $y$ values. This underestimation, attributable to the fact that the peak-locking errors between $u$ and $v$ are uncorrelated, coupled with overestimation of $\sigma_u$ and $\sigma_v$, explains the underestimation of $\rho_{uv}$.

Deviations between the absolute peak-locking case 0A and case IIA are also noted in the two-dimensional plots of $\rho_{uu}$, $\rho_{vv}$, and $\rho_{uv}$ (Fig. 11). Here, the correlation coefficients are shown as a function of both $r_x$ and $y$, with the correlation coefficients computed for case 0A shown in grayscale and those for case IIA shown as line contours. Clearly, the length scales associated with case 0A are smaller than those of case IIA in both $r_x$ and $y$, reinforcing
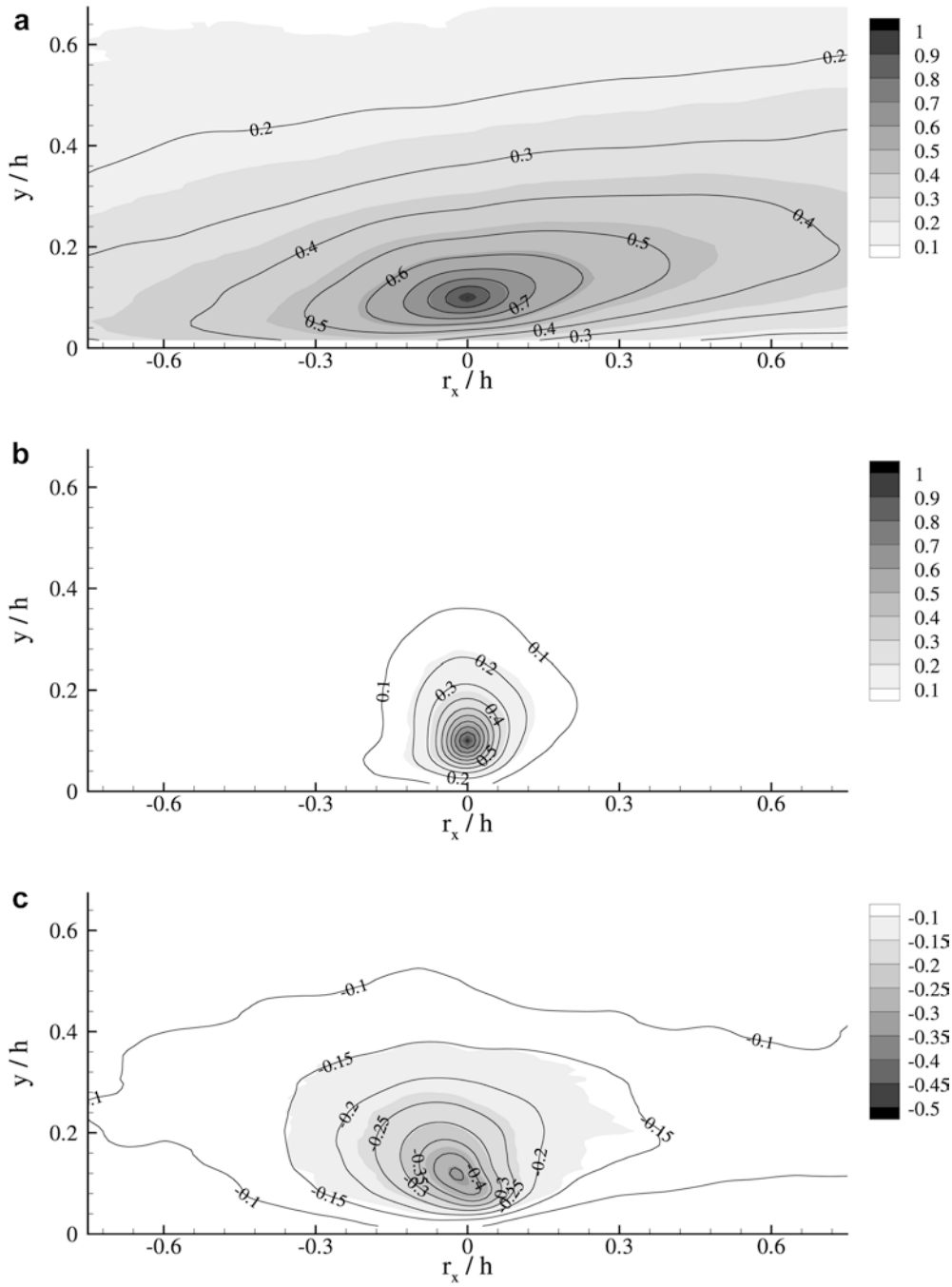
**Fig. 11a–c.** A comparison of two-point velocity correlation coefficients for $y_{\mathrm{ref}}=0.1h$ for case 0A (grayscale contours) and case IIA (line contours). **a** $\rho_{uu}$; **b** $\rho_{vv}$; **c** $\rho_{uv}$

the notion that severely peak-locked data can underestimate two-point correlations significantly, even at larger spatial separations.

# 5
# Influence of displacement dynamic range
In this section, statistics computed from experiment B are compared to those already introduced for experiment A. As noted earlier, the only difference between the two experiments is that the displacement range of B is twice as large as the displacement range of A. Single- and multi-point statistics are compared between the experiments in order to explore the influence of displacement range on statistics computed from peak-locked PIV data.

## 5.1
## Mean velocity
Figure 12 presents the mean velocity profiles for cases 0B (absolute peak locking), case IB (quadratic estimator; moderate peak locking), and case IIB (Gaussian estimator; minimal peak locking). All three profiles collapse with one another and with case IIA (solid line), confirming the insensitivity of the mean profiles to peak-locking influences as is noted in the experiment A data.

## 5.2
## RMS velocities
Figure 13 illustrates the RMS streamwise and wall-normal velocities as computed from the experiment B data. Cases
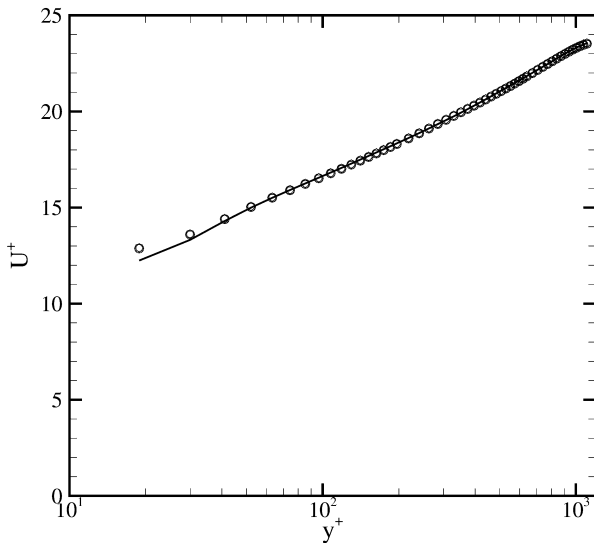
**Fig. 12.** Inner scaling of mean velocity, $U^+$, versus wall-normal position, $y^+$. Cases 0A and IIA are included for comparison. $\diamond$: Case 0B; $\square$: Case IB; $\circ$: Case IIB; $- - -$ : Case 0A; —: Case IIA. (Every other data point is removed for clarity.)

0A and IIA are shown as lines in this figure for comparison. Case 0B overestimates $\sigma_u$ slightly, but not nearly as much as case 0A (plotted as a dashed line). In contrast, cases IB and IIB collapse with case IIA (solid line). The RMS wall-normal velocity is overestimated by case 0B, while cases IB and IIB collapse with IIA. The latter observation is significant because in experiment A, cases I and II deviate moderately in $\sigma_v$ for $y>0.5h$. Therefore, it is clear from this data that the influence of peak-locking errors on the RMS velocities is reduced as the displacement range of the data is increased. In particular, whereas the quadratically estimated $\sigma_v$ data in experiment A fails to collapse with the case IIA data (no peak locking), the quadratically estimated data from experiment B collapses perfectly with IIB despite suffering from moderate levels of peak locking. Additionally, the RMS velocities computed from non-peak-locked data in experiments A and B (cases IIA and IIB) collapse.

As before, the trends noted in the RMS velocities can be understood by considering pdf's of the fluctuating displacements as a function of wall-normal position. Figure 14 presents pdf's of fluctuating streamwise displacement at $y=0.25h$ and $y=0.9h$ for the experiment B data. Comparing these pdf's to those of experiment A (Fig. 16) indicates that the fluctuating streamwise displacements of experiment B span a displacement range that is twice as large as in experiment A. This is to be expected since the PIV time delay in experiment B is twice as large as that in experiment A. In particular, the fluctuating streamwise displacements in experiment B often have magnitudes approaching and exceeding 2 pixels. The magnitudes of fluctuating streamwise displacement rarely exceed 2 pixels in cases IB and IIB; however, a significant number of displacements are locked toward a magnitude of 3 pixels in case 0B. This difference explains the slight overestimation of $\sigma_u$ for case 0B. However, case 0B is certainly in much better agreement than case 0A, where
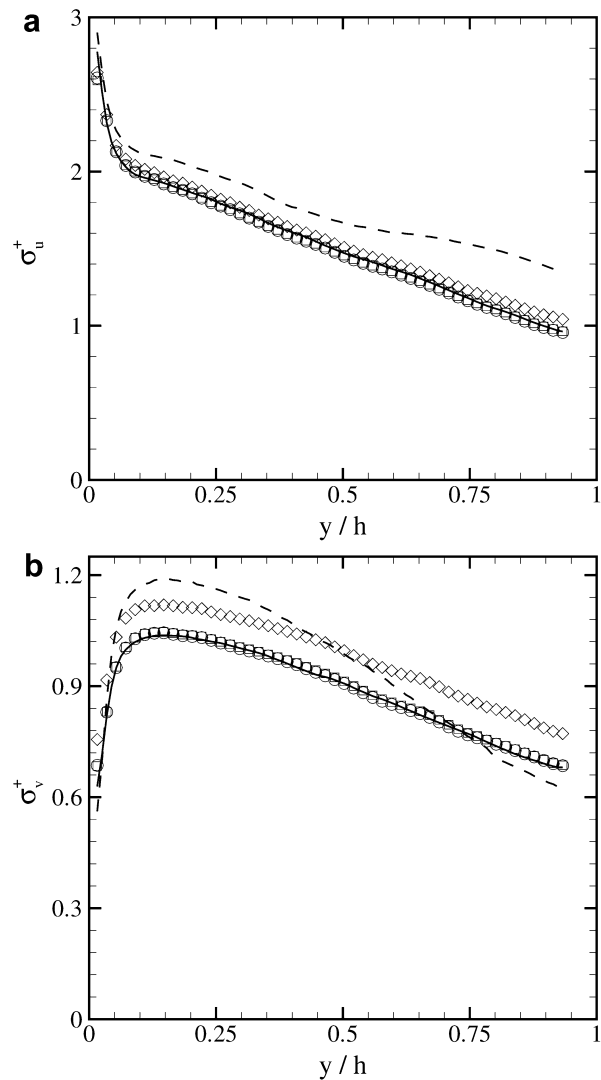




**Fig. 13a,b.** Profiles of RMS velocity as a function of wall-normal position. Cases 0A and IIA are included for comparison. **a** $\sigma_u^+$; **b** $\sigma_v^+$. $\diamond$: Case 0B; $\square$: Case IB; $\circ$: Case IIB; $- - -$ : Case 0A; —: Case IIA. (Every other data point is removed for clarity.)

the displacements are half as large, yielding a severe overestimation of $\sigma_u$. At $y=0.9h$, the fluctuating streamwise displacements are smaller than they are closer to the wall, rarely exceeding 1.5 pixels in cases IB and IIB, but still spanning a broader displacement range than experiment A. This larger range renders $\sigma_u$ less sensitive to peak-locking influences, yielding more accurate estimates of the RMS streamwise velocity.

Figure 15 presents pdf's of fluctuating wall-normal displacement at $y=0.25h$ and $y=0.9h$. As is the case with the fluctuating streamwise displacements, the wall-normal displacements of experiment B span a displacement range that is twice as large as the range in experiment A (Fig. 7). Here, the fluctuating wall-normal displacements exceed 1 pixel in magnitude close to the wall, yielding much better estimates of $\sigma_v$. Near the centerline, the fluctuating wall-normal displacements have magnitudes between 0.5 and 1 pixel. These displacements are locked toward 1 pixel in case 0B, causing an overestimation of $\sigma_v$ in this region of the flow.
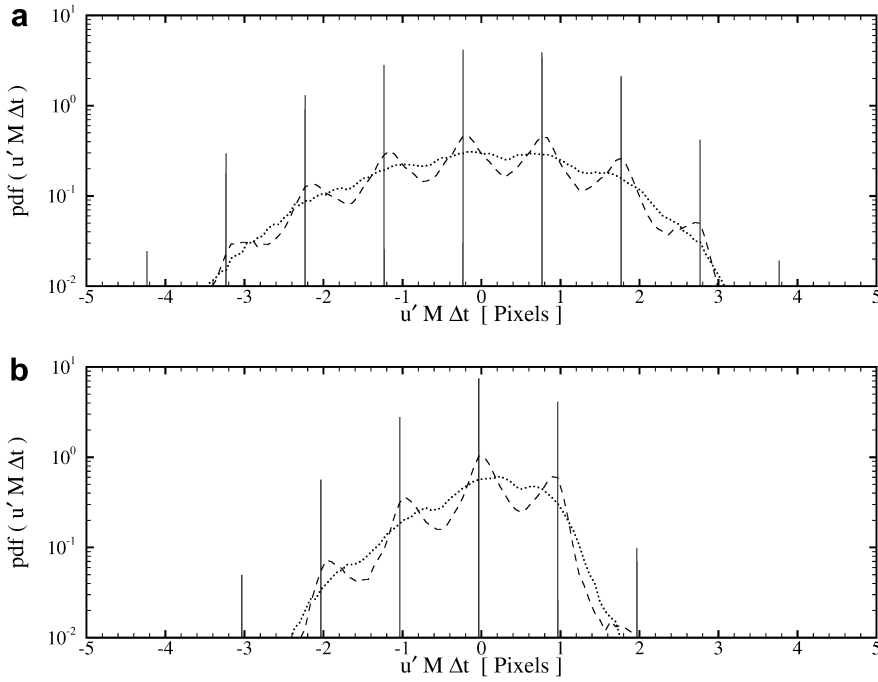
**Fig. 14.** Ensemble-averaged probability density functions of fluctuating streamwise displacement, $u'M\Delta t$, computed from experiment B data at **a** $y=0.25h$ and **b** $y=0.9h$. —: Case 0B; – – –: Case IB; ⋯: Case IIB
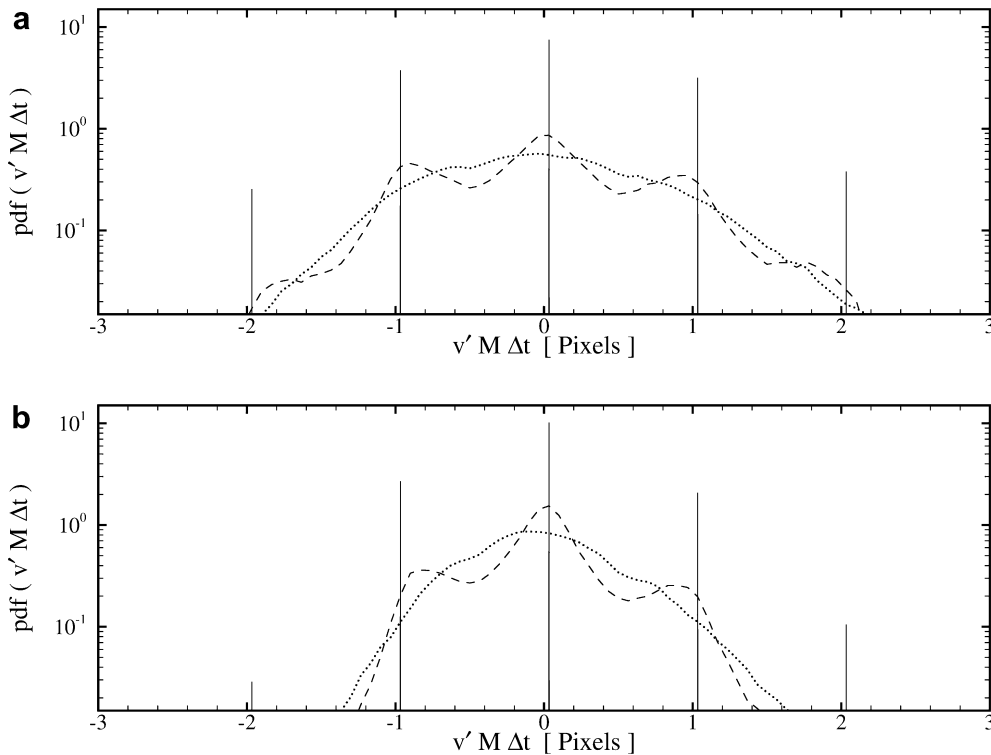


**Fig. 15.** Ensemble-averaged probability density functions of fluctuating wall-normal displacement, $v'M\Delta t$, computed from experiment B data at **a** $y=0.25h$ and **b** $y=0.9h$. —: Case 0B; – – –: Case IB; ⋯: Case IIB

From this analysis, it appears that the RMS velocities are more accurately estimated when the displacement range is larger than when it is smaller. This improvement occurs because the fluctuating displacements are distributed over a larger range of pixel values, rendering the statistics less sensitive to peak locking. In particular, for experiment A (smaller time delay), many fluctuating wall-normal displacements have magnitudes less than

0.5 pixels. These smaller displacements are "locked" toward zero displacement, causing an underestimation of the RMS wall-normal velocity. With a time delay twice as large, the displacements with magnitudes less than 0.5 pixels are spread toward magnitudes closer to 1 pixel in experiment B. This broader displacement range plays a crucial role in the improved accuracy of the experiment B data, especially the improved accuracy of the case I data
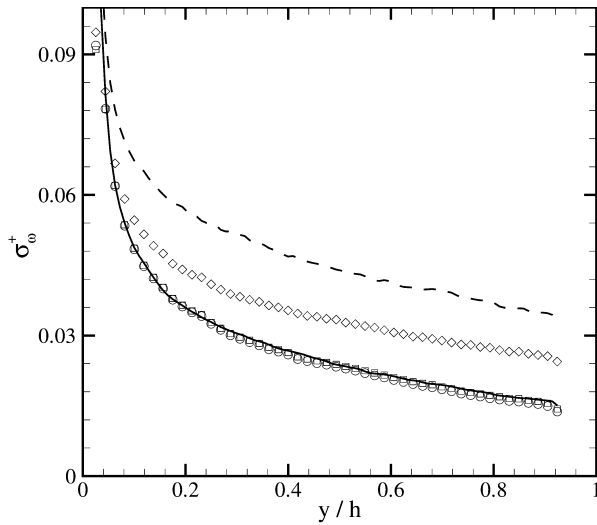
**Fig. 16.** Profiles of RMS spanwise vorticity as a function of wall-normal position. Cases 0A and IIA are included for comparison. ◇: Case 0B; □: Case IB; ○: Case IIB; – – –: Case 0A; —: Case IIA. (Every other data point is removed for clarity.)

(moderate peak locking) as compared to case II (no peak locking). In particular, this broadening yields far fewer displacements locked toward zero.

It should be noted, however, that for extremely long time delays, the velocity fluctuations can be averaged significantly. Therefore, a limit in the size of the displacement dynamic range exists, beyond which the averaging associated with an excessively long time delay will degrade the quality of the measured fluctuations. Clearly this limit is not reached in experiment B since the statistics for cases IIA and IIB match identically.

### 5.3
### Vorticity
Figure 16 illustrates wall-normal profiles of RMS spanwise vorticity for all three cases in experiment B, along with the results from cases 0A and IIA. Cases IB and IIB collapse on one another (and with case IIA), while case 0B deviates significantly. However, the deviation noted with case 0B is not as severe as with case 0A. The improvement seen in the absolute peak-locking case between experiments A and B is again attributable to the broader displacement range in B as compared to A.

### 5.4
### Multi-point statistics
Two-point velocity correlation coefficients computed from the experiment B data are shown in Fig. 17 for all three cases. In addition, the results from cases 0A and IIA are included for comparison. Cases IB and IIB collapse for all three correlations, just as cases IA and IIA did. In addition, the agreement between case 0B and cases IB and IIB is substantially better than it is for case 0A compared to cases IA and IIA (see Fig. 10). The broader displacement range appears to reduce the sensitivity of the two-point correlation coefficients to peak-locking errors. For experiment A, it was found that $\rho_{uu}$ and $\rho_{vv}$ are sensitive to severe peak-locking errors, principally because $\sigma_u$ and $\sigma_v$

are overestimated. Since $\sigma_u$ and $\sigma_v$ in experiment B are more accurately estimated due to the larger displacement range of the data, $\rho_{uu}$ and $\rho_{vv}$ are also more accurate, especially case 0B (absolute peak locking). The streamwise length scales defined by the widths of the correlations in Fig. 17 are also more accurately estimated in the absolute peak-locking case 0B than they are for case 0A.

Deviation in $\rho_{uv}$ is noted between case 0B and cases IB and IIB. However, at zero separation this deviation is only 10%, compared with over 30% in experiment A. Therefore, the broader displacement range of experiment B clearly improves the accuracy of the two-point velocity correlation coefficients, particularly $\rho_{uv}$.

### 6
### Conclusions
The present study indicates that the mean velocity profile is the only statistic that is *insensitive* to peak locking. All other statistics are found to be sensitive to peak-locking errors. In particular, since the mean velocity is unaffected by these influences, the peak-locking errors present in the total velocity are passed on to the measured turbulent velocity fluctuations. Therefore, the RMS velocities, the Reynolds stress, vorticity, and two-point velocity correlation coefficients are all quite sensitive to peak locking, especially in the most severe of circumstances.

It is clear from the analysis presented herein that the strongest sensitivity of turbulence statistics to peak-locking errors occurs when the fluctuating displacements are small. In particular, it is found that fluctuating displacements less than 0.5 pixels in magnitude are consistently locked toward zero displacement, causing underestimation of statistics formed from these displacements. Broadening the displacement dynamic range by a factor of two spreads these displacements closer to a magnitude of 1 pixel, significantly improving the accuracy of the statistics. This effect is most notable in statistics involving the wall-normal velocity component. In wall turbulence, the wall-normal velocity fluctuations are quite small compared to the mean flow and a factor of two smaller than the streamwise velocity fluctuations. The wall-normal fluctuations are therefore most sensitive to the influence of the displacement dynamic range.

Therefore, in situations where turbulent fluctuations are to be measured, great care should be taken to ensure that peak-locking influences are minimized. When peak locking cannot be completely suppressed, due to experimental limitations, for example, one should ensure that the displacements associated with the turbulent fluctuations are larger than 1 pixel in magnitude. This consideration appears to be extremely important since data with moderate peak locking (case IB) still yield accurate turbulence statistics when the magnitude of the displacement fluctuations exceed 1 pixel. However, care must be taken to limit the size of the displacement range. An excessively large displacement range produced by an extremely large time delay can degrade the quality of the measured displacement fluctuations. So, although peak-locking errors may not affect the turbulence statistics, errors associated with excessive averaging in the PIV interrogation due to a large time delay will cause severe underestimation of the
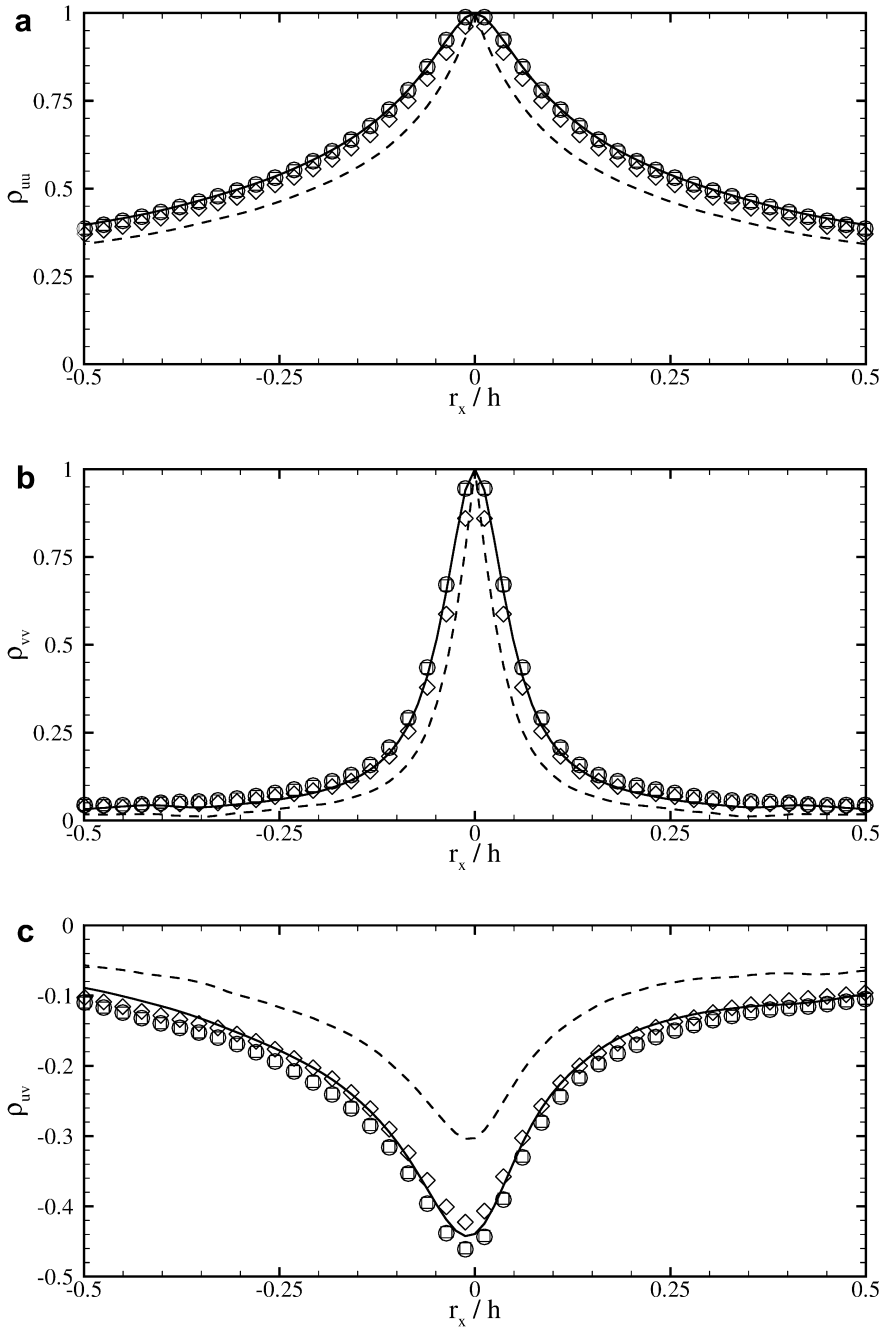
**Fig. 17a–c.** A comparison of two-point velocity correlation coefficients as a function of $r_x$ for $y=y_{ref}=0.1h$ computed from experiment B data. Cases 0A and IIA are included for comparison. **a** $\rho_{uu}$; **b** $\rho_{vv}$; **c** $\rho_{uv}$. ◇: Case 0A; □: Case IA; ○: Case IIB; – – – : Case 0A; ——: Case IIA. (Every other data point is removed for clarity.)

turbulent fluctuations. Therefore, one must find a balance between these two competing influences. Such a balance is achieved between experiments A and B in the present work since the statistics computed from cases IIA and IIB (no peak locking) match identically despite a factor of two difference in time delay.

### References

Christensen KT (2001) Experimental investigation of acceleration and velocity fields in turbulent channel flow. PhD thesis, Department of Theoretical and Applied Mechanics, University of Illinois at Urbana-Champaign, Urbana, Ill.

Christensen KT, Adrian RJ (2002) Measurement of instantaneous Eulerian acceleration fields by particle-image accelerometry:method and accuracy. Exp Fluids 33(6):759–769

Christensen KT, Soloff SM, Adrian RJ (2000) PIV sleuth: integrated particle-image velocimetry (PIV) interrogation/validation software. Technical Report 943, Department of Theoretical and Applied Mechanics, University of Illinois at Urbana-Champaign, Urbana, Ill.

Huang H, Dabiri D, Gharib M (1997) On errors of digital particle image velocimetry. Meas Sci Tech 8(12):1427–1440

Langford J, Moser RD (1999) Optimal LES formulations for isotropic turbulence. J Fluid Mech 398:109–135

Reuss DL, Adrian RJ, Landreth CC, French DT, Fansler TD (1989) Instantaneous planar measurements of velocity and large-scale vorticity and strain in an engine using particle-image velocimetry. Technical report, Society of Automotive Engineers

Roesgen T (2003) Optimal subpixel interpolation in particle image velocimetry. Exp Fluids 35(3):252–256

Westerweel J (1997) Fundamentals of digital particle image velocimetry. Meas Sci Tech 8:1379–1392